# Oxidatively Electrodeposited Thin-Film Transition Metal (Oxy)hydroxides as Oxygen Evolution Catalysts

Carlos G. Morales-Guio, Laurent Liardet, and Xile Hu*

Laboratory of Inorganic Synthesis and Catalysis, Institute of Chemical Sciences and Engineering, École Polytechnique Fédérale de Lausanne (EPFL), 1015 Lausanne, Switzerland

S *Supporting Information*

ABSTRACT: The electrolysis of water to produce hydrogen and oxygen is a simple and attractive approach to store renewable energies in the form of chemical fuels. The oxygen evolution reaction (OER) is a complex four-electron process that constitutes the most energy-inefficient step in water electrolysis. Here we describe a novel electrochemical method for the deposition of a family of thin-film transition metal (oxy)hydroxides as OER catalysts. The thin films have nanodomains of crystallinity with lattice spacing similar to those of double-layered hydroxides. The loadings of these thin-film catalysts were accurately determined with a resolution of below 1 μg cm^{-2} using an electrochemical quartz microcrystal balance. The loading–activity relations for various catalysts were established using voltammetry and impedance spectroscopy. The thin-film catalysts have up to four types of loading–activity dependence due to film nucleation and growth as well as the resistance of the films. A zone of intrinsic activity has been identified for all of the catalysts where the mass-averaged activity remains constant while the loading is increased. According to their intrinsic activities, the metal oxides can be classified into three categories: NiO$_x$, MnO$_x$, and FeO$_x$ belong to category I, which is the least active; CoO$_x$ and CoNiO$_x$ belong to category II, which has medium activity; and FeNiO$_x$, CoFeO$_x$, and CoFeNiO$_x$ belong to category III, which is the most active. The high turnover frequencies of CoFeO$_x$ and CoFeNiO$_x$ at low overpotentials and the simple deposition method allow the fabrication of high-performance anode electrodes coated with these catalysts. In 1 M KOH and with the most active electrode, overpotentials as low as 240 and 270 mV are required to reach 10 and 100 mA cm^{-2}, respectively.
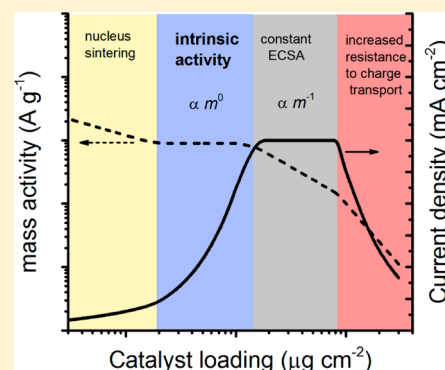
INTRODUCTION

The electrochemical splitting of water into hydrogen and oxygen ($2H_2O \rightarrow 2H_2 + O_2$) provides a promising mechanism for the storage of renewable energies.[1] The oxidative half-reaction of water splitting, the oxygen evolution reaction (OER), $2H_2O \rightarrow 4H^+ + O_2 + 4e^-$, typically requires a larger overpotential than the reductive half reaction, the hydrogen evolution reaction (HER), $2H^+ + 2e^- \rightarrow H_2$.[2] Therefore, the OER is often considered as the bottleneck of water splitting.[3]

The best known OER catalysts are iridium and ruthenium oxides, which are stable under acidic conditions where other metal oxides are unstable and are often used in proton exchange membrane electrolyzers.[4,5] Although IrO$_x$ and RuO$_x$ are also active in alkaline solutions, inexpensive metal oxides based on first-row transition metals are preferred because of their comparable activity and stability under these conditions.[2,6,7]

In recent years, the development of inexpensive metal oxides as catalysts for the OER in alkaline solutions has generated renewed interest.[8–11] A number of such catalysts are reported to be highly active, surpassing IrO$_x$ and RuO$_x$.[12,13] On a molecular level, the activity of a catalyst is best characterized by its apparent turnover frequency (TOF). Boettcher and co-workers reported a solution-cast method for the deposition of

thin metal oxide films with thickness between 2 and 3 nm.[14] A Ni$_{0.9}$Fe$_{0.1}$O$_x$ catalyst was found to be most active, having a TOF of 2.8 s^{-1} at an overpotential (η) of 350 mV. Yeo and Bell[8,15] reported that thin films of CoO$_x$ and NiOOH electrodeposited on gold had TOFs of 1.8 and 1.9 s^{-1}, respectively, at similar overpotentials. We reported an optically transparent FeNiO$_x$ catalyst with a TOF of 1.1–5.0[16] s^{-1} at η = 350 mV.[17] In terms of TOF, these materials are the most active OER catalysts in alkaline solutions.[18] However, they exhibit high TOFs only when the catalyst loading is on the order of 1 μg cm^{-2}. For practical applications, especially in high-current-density electrolyzers (0.5–2 A cm^{-2}), a significantly higher catalyst loading is required to maintain a modest overpotential (e.g., 300 mV). Unfortunately, when the loading of the above catalysts increases, their TOFs substantially decrease. The origin of this decrease is not yet fully understood. Systematic studies of the loading–activity relationship of OER catalysts may reveal the factors that limit the TOF at high mass loadings, guiding the design of more practical catalysts. These studies, however, require the ability to continuously deposit and measure the same catalysts over a wide range of loadings. Here we show that

the combination of electrodeposition and a quartz crystal microbalance (QCM) provides such ability. Consequently, the loading–activity relationships for a series of unary, binary, and ternary metal (oxy)hydroxides have been elucidated. The study leads to an accurate quantification of their intrinsic activities,[19] which reveals the activity trend across first-row transition metal (oxy)hydroxides. Two new superior OER catalysts, $CoFeO_x$ and $CoFeNiO_x$, have been discovered, which can be deposited on high-surface-area supports to catalyze the OER in 1 M KOH with current densities of 10 and 100 mA cm^{-2} at overpotentials of 240 and 270 mV, respectively.

EXPERIMENTAL SECTION

Materials. Sodium acetate (NaOAc, anhydrous, ≥99%), nickel(II) acetate (NiOAc, tetrahydrate, 98%), iron(III) sulfate ($Fe_2(SO_4)_3$, hydrate, 97%), and iron(II) chloride ($FeCl_2$, tetrahydrate, 99%) were purchased from Sigma-Aldrich. Cobalt(II) chloride ($CoCl_2$, anhydrous, >98%) and manganese(II) chloride ($MnCl_2$, tetrahydrate, 97%) were purchased from Fluka. Unless mentioned otherwise, all of the experiments were carried out under normal atmospheric conditions.

Solution Preparation. Millipore deionized water (18.2 MΩ cm) was used to prepare all of the solutions. The concentrations of precursors used in typical electrodepositions of the different catalyst films are shown in Table 1. All of the electrodeposition baths

Table 1. Concentrations of Metal Ion Precursors in Electrodeposition Baths

catalyst	$CoCl_2$	$Fe_2(SO_4)_3$	NiOAc	$MnCl_2$	$FeCl_2$
$CoFeO_x$	16 mM	5 mM			
CoO_x	16 mM				
$FeNiO_x$		5 mM	16 mM		
NiO_x			16 mM		
$CoFeNiO_x$	16 mM	5 mM	16 mM		
$CoNiO_x$	16 mM		16 mM		
MnO_x				16 mM	
FeO_x					16 mM

contained 0.1 M NaOAc as a supporting electrolyte. The pH of the solutions was not adjusted unless otherwise mentioned. Solutions containing iron(III) ions had a pH of 5.3–5.4, and other solutions had pHs of 7.3–7.5. When necessary, the pH of the deposition bath was adjusted using a 0.1 M acetic acid (glacial, VWR) solution.

Catalyst Electrodeposition. All of the electrochemical experiments were carried out using a Methrom Autolab potentiostat/ galvanostat in a three-electrode setup. The substrate for electrodeposition was set as the working electrode, a clean titanium wire was used as the counter electrode, and a Ag/AgCl sat. KCl was used as the reference electrode. In this work, all of the potentials were measured against the Ag/AgCl/sat. KCl reference electrode and are reported against the reversible hydrogen electrode (RHE). The RHE potential was determined using a clean platinum wire in a hydrogen-saturated electrolyte solution. Au-coated 10 MHz quartz crystals were used to determine the catalyst loading in an eQCM 10M quartz crystal microbalance cell. Fluorine-doped tin oxide (FTO) substrates (TEC-15, Nippon Sheet Glass) coated with a sputtered 10 nm Cr adhesion layer and 100 nm Au were also used as electrodeposition substrates and gave results identical to those obtained with the Au-coated quartz crystals. Typically, electrodeposition was performed by consecutive linear sweeps from 1.7 to 2.0 V vs RHE at 10 mV s^{-1}. The current efficiency during the oxidative deposition is the fraction of electrons collected by the working electrode that are involved in the oxidative deposition of the catalyst ($M^{2+}(aq) \rightarrow MOOH(s) + e^- + 3H^+$). The amount of catalyst deposited per cycle was obtained from the change in the mass determined by the eQCM. The most active catalysts were deposited on a nickel foam (thickness 1.6 mm, porosity 95%, Goodfellow Cambridge Limited) by 100 consecutive linear sweeps

between 1.4 and 1.6 V vs RHE. The active area of the nickel foam was delimited and then pretreated in 6 M HCl (37%, VWR) for 10 min prior to the catalyst electrodeposition.

Electrochemical Measurements. A three-electrode setup was used to record current density–potential curves. The conductive substrate with the electrodeposited catalysts was set as the working electrode, a Ag/AgCl sat. KCl electrode was used as the reference electrode, and a platinum wire was used as the counter electrode. Iron-free[20] 1 M KOH solution (Merck) was used to determine the activities of the various films toward oxygen evolution by cyclic voltammetry using a scan rate of 5 mV s^{-1}. Only electrocatalysts deposited on nickel foam were studied at lower potential sweep rates of 1 mV s^{-1} by cyclic voltammetry at current densities below 10 mA cm^{-2} to avoid transient currents due to oxidation and reduction of the catalyst. An H-shaped glass cell was used in order to separate the cathode and anode and avoid the contribution of hydrogen oxidation to the anodic current. In addition, the cell was immersed in a water bath to keep a constant temperature during the experiments. The uncompensated resistance was estimated from the response at high frequencies ($f > 100$ kHz) from electrochemical impedance spectroscopy (EIS).

The electrochemical surface area (ECSA) was measured on Au-coated quartz crystals with different catalyst loadings in 1 M KOH. For all of the catalyst films, the potential was cycled between 1.32 and 1.36 V vs RHE at scan rates of 5, 10, 20, 40, 60, 80, and 100 mV s^{-1}. The current densities ($\Delta j = j_a - j_c$) measured at 1.34 V vs RHE were used to determine the ECSA as the slope of the plot of Δj versus scan rate. Under conditions of a pure capacitive process, this ECSA is equivalent to 2 times the double-layer capacitance (C_{dl}).[21] The ECSA was measured after the measurement of the oxygen evolution activity. The potential window used is important. The ECSA determined at more negative potentials where the catalyst is nonconductive correlates to the ECSA of the substrate but not that of the catalyst.[19] The double-layer capacitance was also determined using EIS, and for some of the materials the C_{dl} value was similar to the ECSA value determined by cyclic voltammetry instead of being half of it. This indicates a pseudocapacitive process in addition to the double-layer capacitance at the potential where EIS was performed. The EIS response of $CoFeO_x$ films was measured every 20 mV between 1.3 and 1.56 V vs RHE in iron-free 1 M KOH solution. The electrode was allowed to stabilize at each potential for 60 s before the EIS measurement. The EIS response was measured from lower to higher potentials. Impedance data were analyzed and fitted using ZView software (Scribner Associates).

The Faradaic yield was measured using a gas-tight H-cell with an optical oxygen sensor (GMP) as previously described.[17] The quantification of oxygen evolved was performed for $CoFeO_x$ and $CoFeNiO_x$ deposited on nickel foam. The uncompensated resistance was measured by EIS before and after each current density measurement.

RESULTS

Anodic Electrodeposition of Transition Metal (Oxy)-hydroxides. We recently reported the anodic electrodeposition of $FeNiO_x$ OER catalysts from iron(III) sulfate and nickel(II) acetate precursors in a mildly acidic aqueous solution (pH 5.3).[17] The high activity of the electrodeposited catalyst for oxygen evolution reduced the local pH, causing corrosion of the film. This resulted in slow and controlled deposition of the catalyst film.

This electrodeposition method was then extended to the deposition of a series of metal oxides, including unary (MnO_x, FeO_x, NiO_x), binary ($CoFeO_x$, $CoNiO_x$), and tertiary ($CoFeNiO_x$) oxyhydroxides. The deposition of CoO_x and $CoFeO_x$ is described in detail here. The amount of material deposited could be controlled by changing the number of deposition cycles (Figure 1a). The time-dependent current efficiency of deposition is shown in Figure 1b. At pH 7.3, the deposition profile of CoO_x is similar to that of NiO_x at the
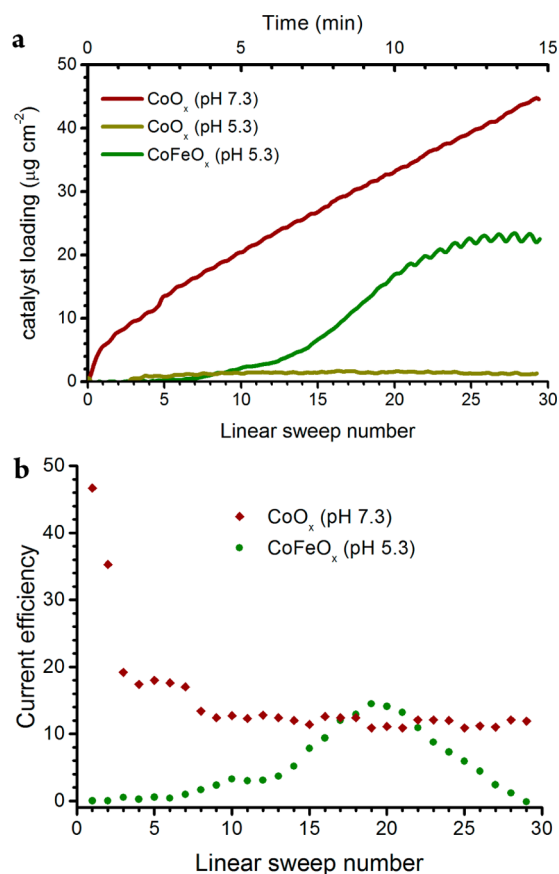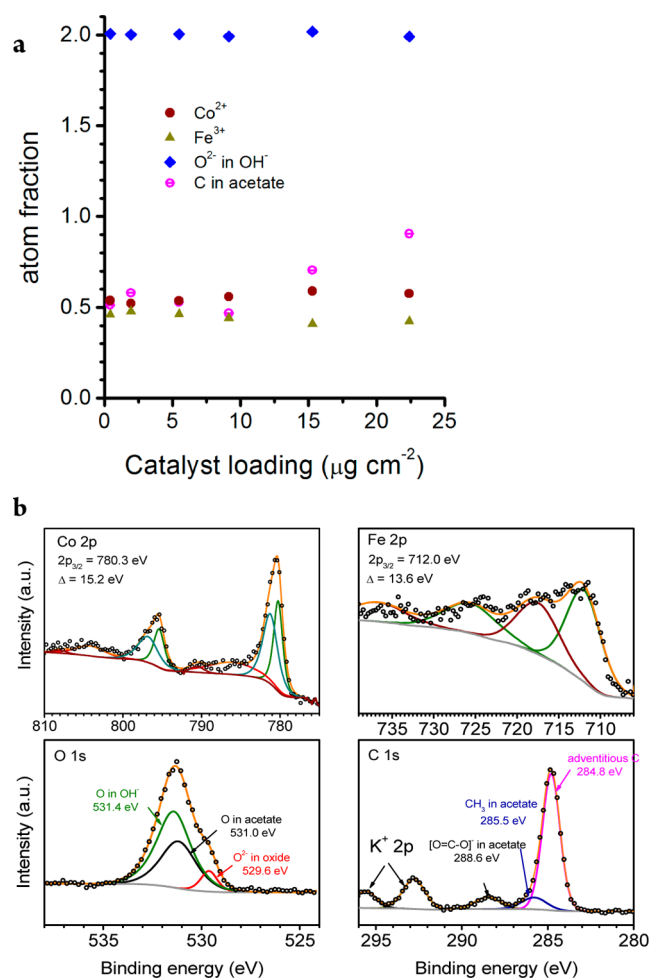
Figure 1. (a) Evolution of the mass of the CoO_x and $CoFeO_x$ films during oxidative deposition. (b) Sweep-number-dependent current efficiency of metal oxide deposition during electrodeposition of the CoO_x and $CoFeO_x$ films.

ratio increases slightly with the number of deposition cycles and loading (Figure 2a). Ex situ XPS shows a Co 2p signal in

Figure 2. Chemical composition of $CoFeO_x$ films. (a) Chemical compositions of the $CoFeO_x$ films at different loadings. (b) XPS spectra of $CoFeO_x$.

same pH.[17] The initial linear sweeps had higher current efficiency than the latter ones because as the film grew it catalyzed oxygen evolution at the deposition potentials, which competed with the oxidative deposition of the catalyst. When the pH was decreased to 5.3, CoO_x could no longer be deposited. When the Fe(III) precursor was added to the Co(II) solution, little material was deposited during the first linear sweeps. However, after five linear sweeps the oxidative deposition started to take place (Figure 1a). When the loading of $CoFeO_x$ reached 15 $\mu g\ cm^{-2}$, the current efficiency for its deposition was similar to that for deposition of CoO_x. However, at higher catalyst loadings the mass of the material deposited started to oscillate and the current efficiency decreased, indicating that corrosion outcompeted deposition. The maximum loading was 20 $\mu g\ cm^{-2}$ for $CoFeO_x$, which is much higher than the maximum loading of 3 $\mu g\ cm^{-2}$ for $FeNiO_x$.[17]

The chemical compositions of the electrodeposited CoO_x and $CoFeO_x$ films were measured by X-ray photoelectron spectroscopy (XPS). The Co 2p signal from the CoO_x catalyst corresponds to that of cobalt in $Co(OH)_2$[22] (Figure S1). The binding energy (BE) of the main Co $2p_{3/2}$ signal was 780.3 eV. Shake-up satellites at higher binding energies, accounting for up to 25% of the total signal intensity, indicate a high-spin Co^{2+} state[23] in the electrodeposited material. The ratio of $OH^- + O^{2-}$ to Co is 1.8:1. No adventitious iron was detected by XPS. In comparison, the Co:Fe ratio in the $CoFeO_x$ film is approximately 0.6:0.4 according to XPS (Figure S2). This

$CoFeO_x$ that corresponds to Co^{2+} in a hydroxide environment with a $2p_{3/2}$ binding energy of 780.3 eV (Figure 2b). Iron is in an oxidation state of +3 (Fe $2p_{3/2}$ at 712.0 eV). The signal in the O 1s region at BE = 531.4 eV corresponds to oxygen atoms similar to that of OH^- in transition metal hydroxides. A smaller signal of more reduced O^{2-} assigned to the lattice oxygen in metal oxides was observed at BE = 529.6 eV. The number of hydroxide ions is approximately twice the number of Co and Fe atoms (Figure 2a). An additional oxygen peak centered at BE = 531.0 eV was also visible in the O 1s region, which was attributed to oxygen of the acetate anion from the supporting electrolyte and other absorbed oxygen species. In addition, the carbon C 1s signal at BE = 288.6 eV was attributed to the carboxyl group in acetate. The acetate signals were observed for the $CoFeO_x$ films even after prolonged oxygen evolution catalysis in 1 M KOH. Potassium ions from the alkaline solution were also observed in the C 1s region despite a thorough washing of the catalyst before XPS analysis. These results could be explained by the fact that layered hydroxides containing bivalent and trivalent transition metals trap anions and water in the interlayers to compensate for the charge of the metal hydroxide layers. The ratio of acetate to Fe^{3+} determined

by XPS for various $CoFeO_x$ films is approximately 1:1 at loadings of up to 10 μg cm^{-2} (Figure 2a). Thus, the chemical composition of the $CoFeO_x$ film might be written as $[Co^{2+}_{1-x}Fe^{3+}_x(OH)_2]^{x+} \cdot (OAc^-)_x \cdot nH_2O$, where x has values between 0.4 and 0.5. At higher loadings, the ratio of OAc^- to Fe^{3+} ions increased. The fraction of cobalt in the material also increased, indicating a composition change at high loadings.

It was hypothesized that the incorporation of iron into CoO_x occurred through a mechanism involving in situ reduction of Fe^{3+} to Fe^{2+} in the counter electrode and subsequent oxidative deposition of iron(II) and cobalt(II) on the working electrode. In situ UV–vis measurements in a quartz UV–vis cuvette fitted with small working, counter, and reference electrodes showed a slow increase in the Fe^{2+} concentration in the solution during the electrodeposition of $CoFeO_x$ (Figure S3). When an Fe(II) precursor was directly used, deposition was unsuccessful, probably because of the fast dissolution of the film in the presence of Fe(II) ions.

Scanning electron microscopy (SEM) showed a porous morphology for $CoFeO_x$ (Figure 3) but a compact morphology
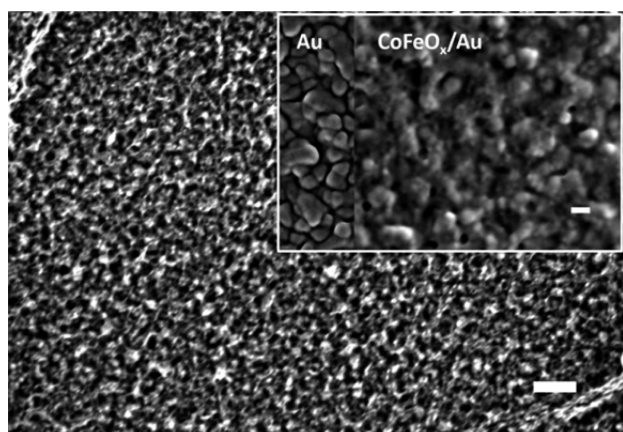
Figure 3. SEM image of a $CoFeO_x$ film electrodeposited on Au-coated FTO (loading = 10 μg cm^{-2}). The scale bar corresponds to 500 nm. The inset shows the porous morphology of the $CoFeO_x$ film compared with the Au-coated substrate before electrodeposition. The scale bar in the inset image corresponds to 100 nm.

for CoO_x. Figure S4 shows the difference in morphology for the electrodeposited $CoFeO_x$ and CoO_x films. The more porous morphology of the $CoFeO_x$ film is correlated with its lower current efficiency during the deposition. During its deposition, the majority of the charges were used to oxidize water, which lowered the pH of the solution and led to partial dissolution of $CoFeO_x$. This, together with the transport of oxygen bubbles out of the catalyst film, might be the origin of pore formation.

The electrochemical surface areas (ECSAs) of the CoO_x and $CoFeO_x$ films at different loadings were determined using cyclic voltammetry (Figure S5). Esswein et al.[24] estimated that there are 6.1×10^{14} surface Co atoms cm^{-2} in cobalt oxide. If it is assumed that each Co atom in the surface participates in the electrochemical surface area measurement, an ECSA of 0.1 mF cm^{-2} would be expected for one active cobalt oxide monolayer. At low catalyst loading, an ECSA of $\sim$0.5 mF cm^{-2} was measured for the $CoFeO_x$ film, and this value increased to 1.0 mF cm^{-2} for loadings between 5 and 20 μg cm^{-2}. This is 1 order of magnitude higher than the value expected for a flat surface. The constant ECSA value at loadings of 5 to 20 μg cm^{-2} indicates that new mass is deposited on the existing

porous active area and that new surface is not being created. Higher ECSA values were obtained at loadings higher than 20 μg cm^{-2}. This correlates to a change in the morphology and composition of the films at higher loadings (vide supra). A CoO_x film with a loading of 5.5 μg cm^{-2} has a similar ECSA of $\sim$1.0 mF cm^{-2} compared to $CoFeO_x$ films with identical loadings (Figure S5). However, values of up to 12.3 mF cm^{-2} (more than 100 monolayers) are measured for thicker CoO_x films with loadings of 30 μg cm^{-2}. Therefore, for CoO_x, the ECSA increases proportionally to the mass of the loading. Dau and co-workers previously observed a similar phenomenon and demonstrated that the bulk of CoO_x is infiltrated by the electrolyte and is electrochemically active.[25] This seems not to be the case for $CoFeO_x$, where only the surface but not the bulk is electrochemically active for the OER.

Other films of unary (MnO_x, FeO_x, NiO_x), binary ($CoNiO_x$), and ternary ($CoFeNiO_x$) oxyhydroxides were also electrodeposited using similar oxidative electrodeposition conditions. NiO_x and MnO_x exhibit a nanosheet morphology with pore sizes on the order of 10–20 nm (Figure S6). The MnO_x film additionally contains particle islands, which were not observed for the other materials. The binary $CoNiO_x$ and ternary $CoFeNiO_x$ had a more compact film morphology with pore sizes smaller than for NiO_x.

The $CoNiO_x$ catalyst has a morphology and composition similar to CoO_x. The Co:Ni ratio is 0.96:0.04. Addition of the Fe(III) precursor in the deposition bath resulted in the formation of a $CoFeNiO_x$ catalyst. The film is a ternary (oxy)hydroxide that is rich in cobalt with a Co:Fe:Ni ratio of 0.50:0.40:0.10 as determined by XPS (Figure S7). Importantly, catalyst loadings of up to 70 μg cm^{-2} can be achieved for the $CoFeNiO_x$ material using the method reported here.

Comparison of OER Activities. The electrocatalytic oxygen evolution activities of the metal oxide films were studied in iron-free 1 M KOH. Figure 4 shows the polarization curves of the films at a loading of 5 μg cm^{-2}. $CoFeO_x$ was found to be the most active catalyst.

The activities of $CoFeO_x$ at different loadings were then determined. The films at loadings between 5 and 10 μg cm^{-2}
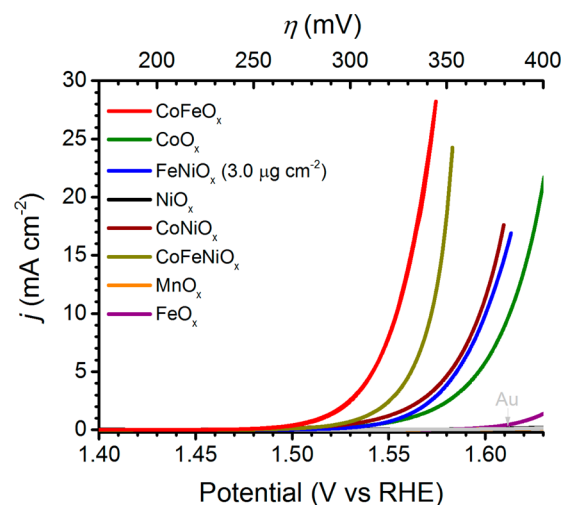
Figure 4. Current density–potential curves for unary, binary, and ternary metal oxides at a catalyst loading of 5.0 μg cm^{-2}, except for $FeNiO_x$, for which the curve at its maximum loading of 3 μg cm^{-2} is shown. Conditions: Au substrate, iron-free 1 M KOH, and a scan rate of 5 mV s^{-1}.

had the highest activities, reaching current densities of 10 mA cm^{-2} at overpotentials between 320 and 330 mV (Figure S8). Lower and higher catalyst loadings resulted in lower current densities at the same overpotentials (Figure S8). The relation between the loading and the OER performance of gold-supported CoO_x films was previously studied by Yeo and Bell.[8] It was suggested that the high work function of gold enhanced the activity of the first layers of CoO_x, but this effect decreased with increasing loading. However, other parameters such as the morphology and conductivity of the catalyst might influence the loading dependence of the activity as well.[26,27] To further analyze the loading–activity relationship, a log–log plot of the apparent turnover frequency (TOF_{app}) at η = 350 mV versus the mass loading was constructed (Figure 5a). The apparent
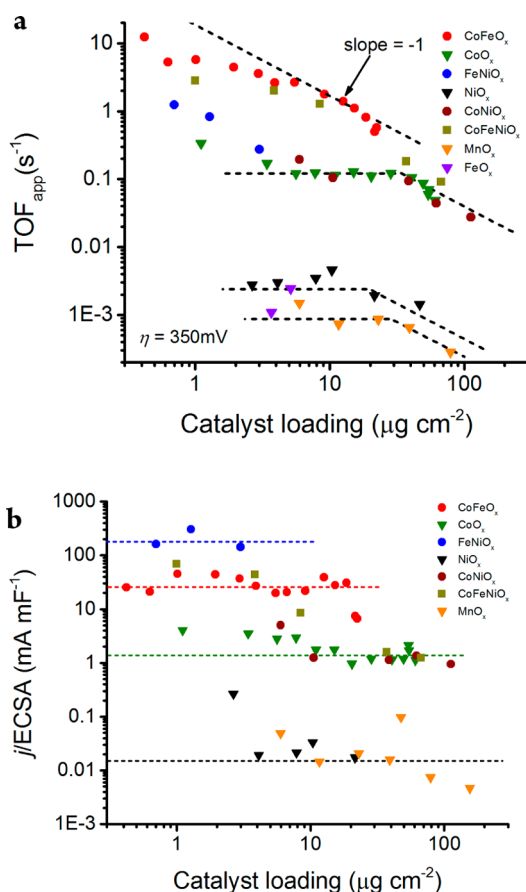
Figure 5. (a) Log–log plots of turnover frequency vs catalyst loading. The TOFs were determined at an overpotential of 350 mV in iron-free 1 M KOH. (b) Activity per electrochemical surface area at η = 350 mV for catalysts at different loadings. The ECSA was determined by cyclic voltammetry for all of the metal (oxy)hydroxides.

turnover frequency of a catalyst ($TOF_{app} \propto j/m$) is proportional to the current density and inversely proportional to the loading (m). For the calculation of apparent TOFs, Fe was assumed to be the only active metal in the $CoFeO_x$, $FeNiO_x$, and $CoFeNiO_x$ films, in agreement with recent reports.[28−30] An analogous log–log plot of mass-averaged activity at η = 350 mV versus mass loading was also constructed without consideration of the active metal ions in the catalysts (Figure S9).

The log–log curve for $CoFeO_x$ is shown as red full circles in Figure 5a. The TOF_{app} is 12 s^{-1} at a loading of 0.4 μg cm^{-2}. The TOF gradually decreases as the loading increases. At

intermediate loadings (5 and 20 μg cm^{-2}), a slope of −1 is observed. At these loadings, the electrodeposition does not create more electrochemical surface area but simply deposits new material to replace the existing active material (see above, Figure S5). This results in the current density being constant and independent of the catalyst loading. Thus, $TOF_{app} \propto 1/m$, which explains the slope of −1 observed in the log−log plot. At even higher loadings, the slope in the log−log curve becomes more negative than −1, indicating an inverse relation of current density with the catalyst loading of a higher order.

For CoO_x at loadings of 5 to 50 μg cm^{-2} (green triangles in Figure 5a), the TOF is independent of the loading. This result indicates that electrodeposition creates new and more surface area . The same trend was observed for NiO_x, FeO_x, MnO_x, and $CoNiO_x$ at intermediate loadings. At high catalyst loadings, the TOFs of these catalysts decrease as the loadings increase, with a slope of −1 in the log(TOF)−log(loading) plot.

The TOF−loading correlation allows an accurate comparison of the activities of the various catalysts. The TOF_{app} of NiO_x in an iron-free 1 M KOH solution is <0.005 s^{-1} at η = 350 mV. FeO_x and MnO_x have TOFs in the same range as NiO_x. These unary metal oxide films are poor catalysts. The activity of CoO_x is independent of whether the electrolyte solution contained Fe impurities. CoO_x and $CoNiO_x$ have similar activities and are ranked at the second class in the group of metal oxides. The first-class catalysts include $CoFeO_x$, $FeNiO_x$, and $CoFeNiO_x$, with $CoFeO_x$ being most active over the whole loading range.

To separate the influence of electrochemical surface area from the influence of other parameters, the current density at η = 350 mV divided by the ECSA measured by cyclic voltammetry was plotted against the catalyst loading (Figure 5b). For all of the catalysts except $CoFeNiO_x$, the ECSA-normalized activity is largely independent of the loading. Per ECSA unit, $FeNiO_x$, $CoFeO_x$, and $CoFeNiO_x$ are again the most active catalysts.

Electrochemical Impedance Spectroscopic Analysis of $CoFeO_x$ Catalysts. EIS was used to probe the origin of the decrease in TOF at high loadings of $CoFeO_x$. An angular frequency window between 0.5 Hz and 500 kHz (corresponding to processes with time constants between 2 s and 2 μs, respectively) was chosen to study the $CoFeO_x$ catalyst. The movements of electrons on conductive materials and ions in electrolytes are fast processes and appear in the high-frequency range of the EIS spectra. Electrochemical reactions on the surface of the electrode are observed at middle and low frequencies, and the characteristic time constant of the charge transfer process decreases with increasing overpotential.

Scheme 1 shows the different EIS models that describe the metal (oxy)hydroxides depending on the morphology and electronic characteristics of the various components. Model (a) was used by Doyle and Lyons[31] to study the EIS response of hydrated metal oxide catalysts. R_s is the uncompensated solution resistance, which also accounts for the resistance to the transport of electrons in the conductive Au substrate. C_c is the capacitance of the first layers of the film in contact with the gold substrate. R_c is the resistance to charge transfer at the back contact. C_{CT} is the double-layer capacitance of the catalyst surface where the OER occurs, and R_{CT} is the corresponding resistance to charge transfer through the catalyst−electrolyte interface during the OER. The capacitance and charge transfer resistance of the Au substrate in contact with the electrolyte are also included in model (a). However, in the fitting of the impedance data this component was dismissed because of the

Scheme 1. Equivalent Circuit Models Used To Fit the EIS Responses of CoFeO$_x$ Films at Different Loadings[a]

Model (a):   **Model (b):**
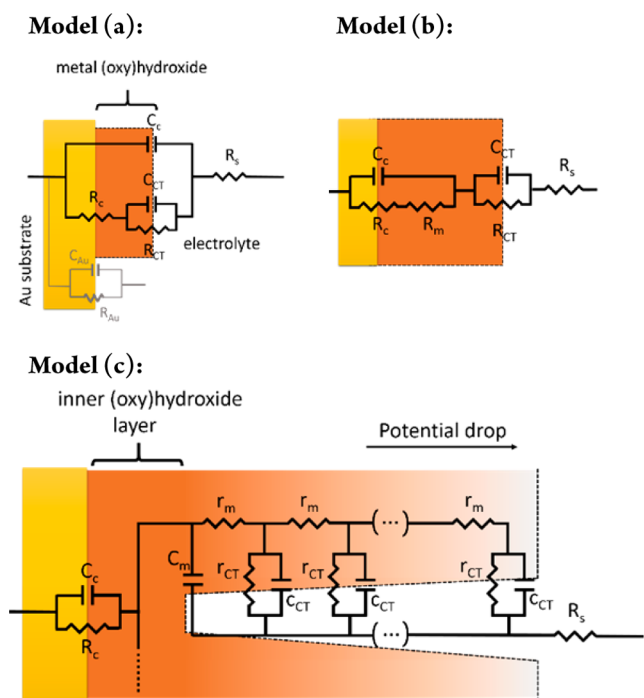
Model (c):

[a]Model (a) corresponds to a very thin film. Model (b) corresponds to a catalyst film where the material in contact with the substrate is not directly involved in the catalytic reaction. Model (c) is a transmission line model for porous catalyst films where the charge transfer process occurs along the length of the pores and there is a potential drop through the film due to a measurable resistance to charge transport and a decrease in the population of catalytic states.

low catalytic activity of Au for OER in the potential window studied.

In model (b), the capacitance at the substrate–catalyst film interface is considered to be different from the capacitance at the catalyst film–electrolyte interface. This is expected for a compact film where there is a measurable resistance to charge transfer R_m from one layer to the next.

A transmission line model is incorporated in model (c). Such a model has been previously used to describe the electrochemical behavior of conductive polymers,[32] amorphous molybdenum sulfide particles during hydrogen evolution,[33] and porous electrodes where electrochemical reactions take place in the walls of the pores throughout the depth of the electrodes.[34,35] This model considers that for a porous catalyst film charge transfer reactions can occur anywhere in the film, while the resistance of the film r_m causes a potential drop along the film thickness.[36] The total resistance of the film is R_m, and the electronic capacitance of the film is C_m.

Figure 6a shows the EIS response of a CoFeO$_x$ film at a loading of 0.4 μg cm^{-2}, fitted using model (a) in Scheme 1. At this very low loading, the coverage of the substrate is around one monolayer. The Bode plot in Figure 6a is dominated by a charge transfer process at middle and low frequencies related to the charge transfer in the catalyst–electrolyte interface. At an overpotential of ~210 mV the oxidation of water begins, and the resistance to charge transfer decreases with a Tafel slope of 37 mV decade^{-1} (Figure 6a, right). The charge transfer capacitance C_{CT} increases with the overpotential, which might be due to the increased chemical pseudocapacitance of the

catalytically active sites when more oxidized intermediates in the OER become accessible at higher overpotentials (vide infra). The phase Bode plot in Figure 6a shows a shoulder at frequencies between 10 and 100 kHz associated with the fast charge transport between the Au substrate and the catalyst film. This component was observed as a semicircle at high frequencies in the Nyquist plot in Figure 6a. The resistance to electron transfer from the substrate to the first layer of the catalyst film (R_c) remains largely potential-independent, suggesting a nonrectifying, close to Ohmic contact between the thin film and the Au substrate. The electronic capacitance of the contact C_c increases with the potential and becomes the same as that of the capacitance to charge transfer (C_{CT}) at overpotentials higher than 210 mV. This is expected for a very thin film where all of the electrochemically active sites have an almost Ohmic contact with the substrate and where the discharge of the chemical capacitor (C_{CT}) occurs through a slow electrochemical process ($R_{CT} \gg R_c$). At this monolayer loading, the catalyst behaves like a metal catalyst, with a TOF$_{app}$ of up to 12 s^{-1} at η = 350 mV.

The EIS response of a CoFeO$_x$ film at a loading of 1.9 μg cm^{-2} (Figure 6b) was fitted using model (b) in Scheme 1. The resistance to charge transfer at the Au–film interface R_c at high frequencies decreases with applied potential, while its time constant (τ_c) remains constant. This behavior is suggestive of an adaptive contact between the substrate and the catalyst film where charges in the C_c region are accumulated through a fast potential-independent process (R_c) and dispersed through a similarly fast potential-dependent process (R_m).[37] Thus, the response at high frequencies was attributed to electron transport through a thin film whose resistance is non-negligible. R_m and R_c could not be differentiated in the EIS analysis and were treated as R_c in Figure 6b. The capacitance at the Au–film interface is smaller than the capacitance at the catalyst–electrolyte interface C_{CT}. Thus, model (b) is better suited than model (a) for the fitting of the EIS data. At this loading, the Tafel slope for the charge transfer process (OER) is also 37 mV decade^{-1}.

Figure 6c shows the EIS response for a CoFeO$_x$ film at a loading of 9.1 μg cm^{-2}. This loading is in the region where the electrochemical surface area is constant and the highest current density for the catalyst is obtained. The Nyquist plot in Figure 6c shows one semicircle at frequencies below ω = 4 kHz attributed to the OER process and a second component at ω > 4 kHz that decreases with overpotential and appears as a flattened semicircle. The high-frequency component was assigned to the combined response of the Au–film interface and the transmission line behavior for a porous catalyst film. The contribution of the transmission line component was more evident for thicker films, e.g., the films at 15.3 μg cm^{-2} (Figure S10) and 21.6 μg cm^{-2} (Figure 6d). For these films, the resistance to electron transport within the film was clearly identified as an EIS response between 0.5 and 6 kHz (Figure S11). The increased resistance in thick films was reflected in an increase in the apparent Tafel slopes determined from voltammetry data (Figure S12). On the other hand, the Tafel slopes determined by EIS remain nearly constant at all loadings (Figure S12) because it is possible to separate charge transport and charge transfer in EIS analysis.[33] The EIS analysis also shows that the capacitance for charge transfer increases with overpotential, which is attributed to the accumulation of more oxidized intermediates at the catalyst–electrolyte interface. The capacitance C_{CT} for the most active catalysts (e.g., Figure 6c)
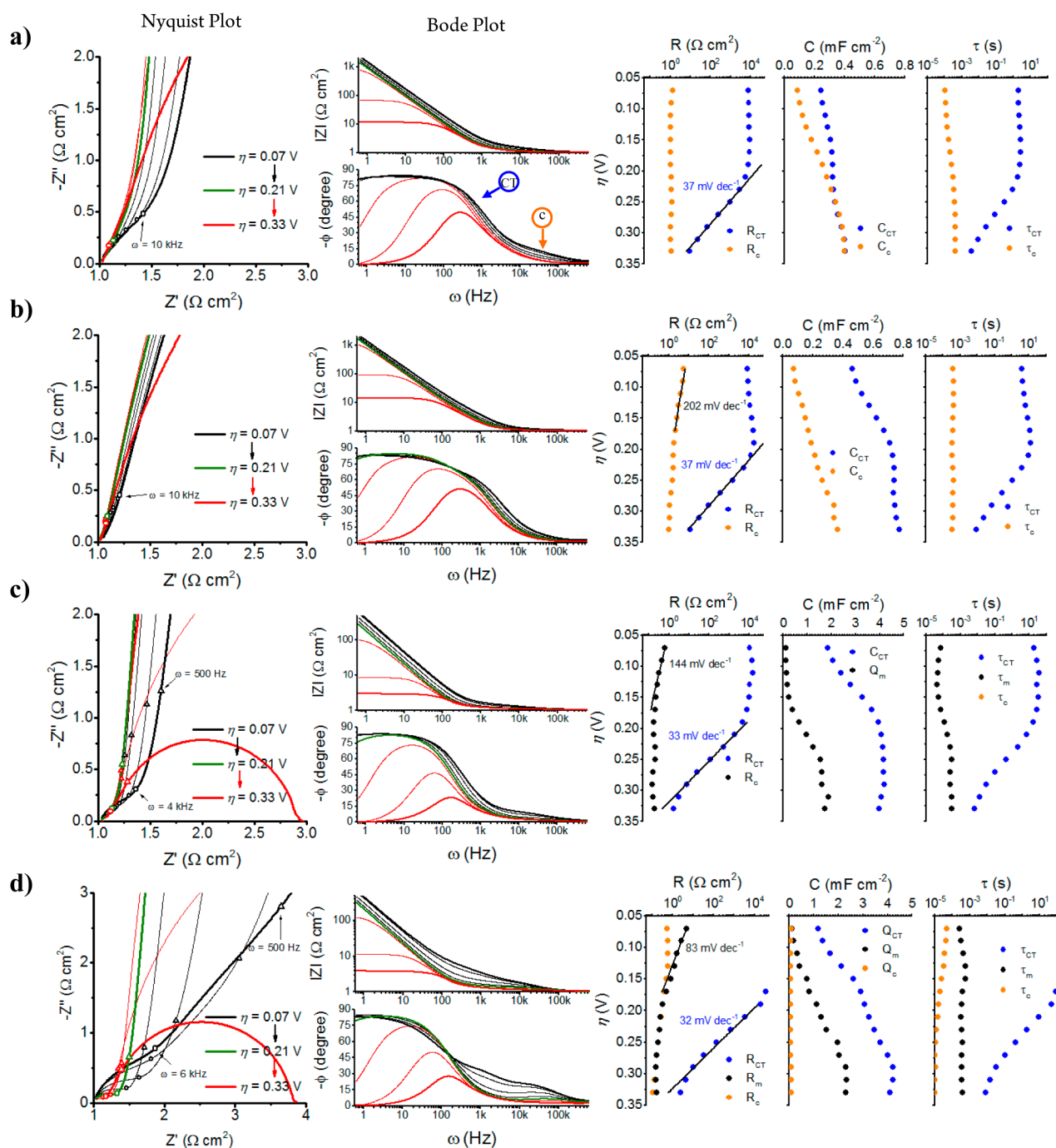
Figure 6. EIS response and fitting parameters of $CoFeO_x$ films at loadings of (a) 0.4, (b) 1.9, (c) 9.1, and (d) 21.6 μg cm^{-2}. Conditions: Au substrate, iron-free 1 M KOH. The EIS response was measured every 20 mV between 1.3 and 1.56 V vs RHE. Selected frequencies are shown in the Nyquist and Bode plots for reference. In the Nyquist and Bode plots, the EIS responses at $\eta = 0.07$ V and every 40 mV between $\eta = 0.09$ V and $\eta = 0.19$ V are shown in black. The response at $\eta = 0.21$ V is shown in green, and the responses every 40 mV between $\eta = 0.25$ V and $\eta = 0.33$ V are shown in red. In the Bode plots, the frequency regions for the different phenomena of charge transfer at the catalyst−electrolyte interface (CT) and charge transfer at the back contact (c) are indicated.

becomes constant after the onset of water oxidation at $\eta \sim 0.2$ V, suggesting that the whole catalyst surface is active for the OER (Figure S13). On the other hand, the capacitance for charge transfer in thick films (e.g., Figure 6d) continues to increase with increasing overpotential, suggesting that a larger fraction of the catalyst surface becomes active for the OER at larger overpotentials.

Construction of High-Surface-Area Anode Materials. Among the three most active catalysts, the maximum loading of

$FeNiO_x$ on a flat Au substrate is 3 μg cm^{-2}, while the maximum loadings of $CoFeO_x$ and $CoFeNiO_x$ are 20 and 70 μg cm^{-2}, respectively, using the anodic electrodeposition method. For high-current-density applications, a high loading of highly active catalysts is required. Thus, $CoFeO_x$ and $CoFeNiO_x$ were further deposited onto nickel foam (NF). After deposition, the nickel foam surface was covered by a layer of rough film with a morphology similar to that observed in the flat substrates (Figure 7a). Catalyst films could be detached from the nickel
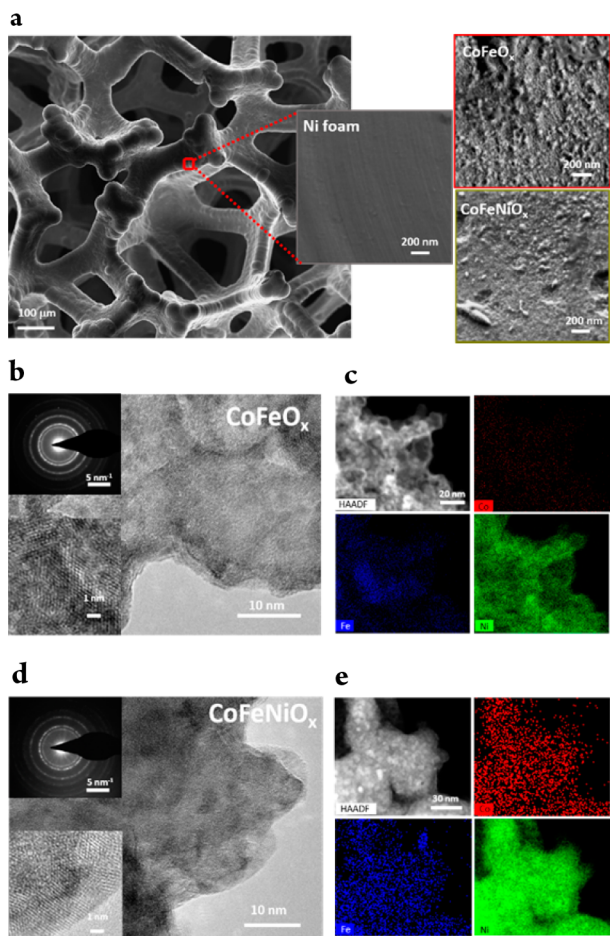
Figure 7. (a) SEM image of nickel foam before and after electrodeposition of the CoFeO$_x$ and CoFeNiO$_x$ catalysts. (b) TEM image and (c) elemental mapping of the CoFeO$_x$ catalyst detached from the nickel foam substrate. (d) TEM image and (e) elemental mapping of CoFeNiO$_x$. The insets in (b) and (d) show the electron diffraction patterns (top left) and HRTEM images (bottom left) of the CoFeO$_x$ and CoFeNiO$_x$ films, respectively.

foam by sonication of the electrode in methanol (Figure S14). High-resolution transmission electron microscopy showed that the CoFeO$_x$ film has small crystalline domains (Figure 7b). The electron diffraction pattern of CoFeO$_x$ (inset in Figure 7b) exhibits features corresponding to lattice spacings of 0.265, 0.218, and 0.156 nm, which could be assigned to the (012), (015), and (110) planes in Co−Fe hydroxide hydrates (JCPDS 50-0235). Elemental mapping shows that Co and Fe are homogeneously distributed in the film (Figure 7c). Nickel is also observed in the film. These nickel species were likely from the nickel foam substrate.

Crystalline nanodomains were also observed for the CoFeNiO$_x$ film (Figure 7d). Lattice spacings of 0.246, 0.212, and 0.149 nm were found, which could be indexed to the (111), (103), and (301) planes of the hexagonal phase of nickel hydroxide hydrate (JCPDS 22-0444). Similar lattice spacings were observed for nickel iron layered double hydroxide (LDH).[38] The ternary oxide shows a homogeneous distribution of Co, Fe, and Ni (Figure 7e).

Both metal oxide electrocatalysts deposited on nickel foam are rich in nickel because of the chemical instability of the substrate under acidic solutions. Some nickel dissolves to form

nickel ions in the deposition bath, which are then incorporated into the metal oxide films during electrodeposition.

The high-surface-area electrodes were tested for the electrochemical OER. In 1 M KOH, current densities of 10 and 100 mA cm^{-2} were reached at overpotentials of 260 and 300 mV for the CoFeO$_x$/NF catalyst. The CoFeNiO$_x$/NF is slightly more active and requires overpotentials of 240 and 270 mV to reach the same current densities (Figure 8). These are
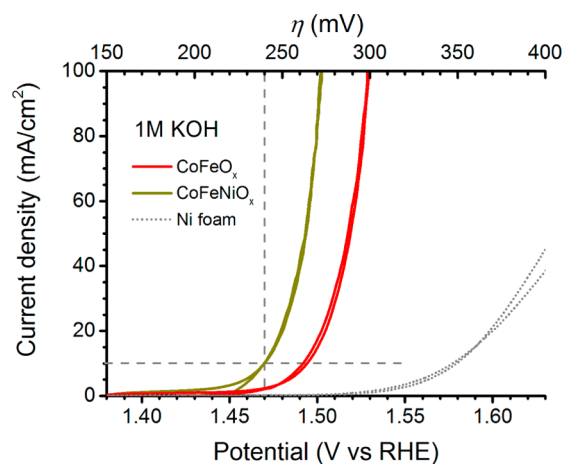

Figure 8. Current density−potential curves for metal oxide catalysts on Ni foam.

among the lowest overpotentials reported for the OER in 1 M KOH (Table S1). Nickel foam itself requires a much larger overpotential. The Tafel slopes were 36 mV decade^{-1} for CoFeO$_x$/NF and 32 mV decade^{-1} for CoFeNiO$_x$/NF. The ECSA of CoFeNiO$_x$/NF was 3.7 mF cm^{-2}, while that of CoFeO$_x$/NF was 1.65 mF cm^{-2}. The Faradaic efficiency for oxygen evolution is close to 100% (Figure S15).

■ DISCUSSION

Anodic Electrodeposition of Transition Metal (Oxy)-hydroxides. The oxidative electrodeposition of an FeNiO$_x$ catalyst had been previously described by our group.[17] However, the deposition mechanism was not well understood, and the implications for the electrodeposition of other mixed metal oxides containing iron had not been explored. The oxidative deposition of unary nickel, cobalt, iron, and manganese oxides[39] from acetate-buffered solutions onto conductive substrates is well-understood[40] and is commonly used to prepare porous coating layers. The deposition mechanism involves one-electron oxidation of the low-valence M^{2+} ion adsorbed on the surface of the electrode ($M^{2+}(aq)_{ads}$) with concomitant precipitation of the (oxy)hydroxide species (eqs 1 and 2):

$$M^{2+}(aq)_{ads} \rightleftarrows M^{3+}(aq)_{ads} + e^- \qquad (1)$$

$$M^{3+}(aq)_{ads} \rightleftarrows MO(OH)(s) + 3H^+ \qquad (2)$$
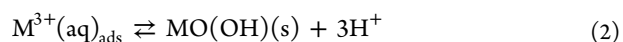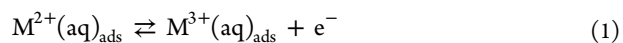
These unary metal oxides catalyze water oxidation in alkaline solutions, but with low intrinsic activities. The intentional and unintentional introduction of iron into Ni and Co films has been shown to significantly increase the activity of unary oxides.[29,41,42]

Metal hydroxides can also be electrodeposited under reductive potentials. The mechanism of cathodic deposition

involves reduction of nitrate anions in the solution (eq 3), thereby increasing the local pH near the working electrode, which leads to precipitation of metal hydroxides (eq 4):[40,43]

$$NO_3^- + H_2O + 2e^- \rightarrow NO_2^- + 2OH^- \qquad (3)$$

$$M^{2+} + 2OH^- \rightarrow M(OH)_2(s) \qquad (4)$$
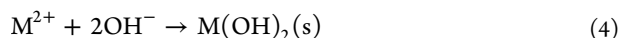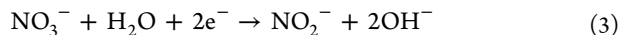
Compared to cathodic deposition, the anodic deposition method described here is potentially advantageous because its electropolymerization mechanism ensures sufficient conductivity of the resulting oxides. When the conductivity of the oxides decreases, the electrodeposition rate diminishes, resulting in a self-limiting growth process. This is indeed observed during the electrodeposition of the $CoFeO_x$ catalyst in Figure 1.

The anodic deposition of binary and ternary metal oxides containing iron has been difficult. The reduction potentials[44] increase in the order H^+/H_2 (0.0 V) < Fe^{3+}/Fe^{2+} (0.77 V) < O_2/H_2O (1.23 V) < Mn^{3+}/Mn^{2+} (1.5 V) < Co^{3+}/Co^{2+} (1.82 V) < Ni^{3+}/Ni^{2+} (calculated as 2.3 V). Thus, starting from Fe^{2+}, unary iron oxide would be deposited before other metal oxides could form, making it impossible to make mixed oxides. Here we solved the problem by introducing a Fe^{3+} precursor into the electrodeposition bath. Scheme 2 shows the proposed

Scheme 2. Proposed Mechanism for the Electrodeposition of $CoFeO_x$[a]
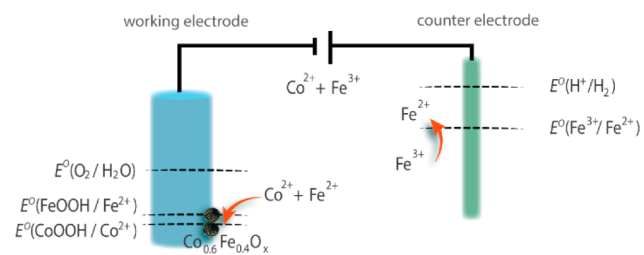
[a]Fe^{3+} is first reduced to Fe^{2+} in the counter electrode. Subsequently, $CoFeO_x$ is oxidatively electrodeposited on the working electrode.

deposition mechanism for the oxidative electrodeposition of $CoFeO_x$ films. During the first linear sweeps, the divalent metal ion is oxidized at the working electrode while Fe^{3+} is reduced in the counter electrode to Fe^{2+}, as observed by in situ UV−vis spectroscopy (Figure S3). The delay in the start of the deposition and the low current efficiency in the first linear sweeps during the deposition of $CoFeO_x$ and $FeNiO_x$ are due to the chemical instability and fast dissolution of the cobalt and nickel oxides under the slightly acidic conditions (Figure 1). Once Fe^{2+} ions diffuse from the counter electrode to the working electrode, electrodeposition of $CoFeO_x$ begins, as observed by the increase in the mass of the quartz crystal. When a significant amount of catalyst is deposited on the working electrode, the oxidation of water decreases the local pH. The deposition of new material is balanced by its dissolution. The growth of the catalyst film then stops. The maximum loading of a catalyst is also limited by the conductivity of the film. Iron-rich catalysts are more insulating, resulting in thinner films. As an example, the Fe-rich catalyst $FeNiO_x$ has a maximum loading of about 3 $\mu g\ cm^{-2}$; this is much lower than that of $CoFeNiO_x$, which has a lower iron content and a maximum loading of about 70 $\mu g\ cm^{-2}$.

The electron diffraction patterns of $CoFeO_x$ and $CoFeNiO_x$ films exhibit features arising from in-plane lattice spacings of

LDHs but not their characteristic d spacings along the z axis. This result indicates that these catalysts have a local structure similar to LDH, even though they do not stack to form large crystals in the z direction. Nickel-, cobalt-, and iron-containing double-layered hydroxides have recently received much attention because of their promising OER activity.[38] This work provides a convenient electrodeposition method for the synthesis of these double-layer hydroxides.

Loading-Dependent Activity. The chemical compositions of the metal oxides do not change significantly during the anodic electrodeposition, indicating that the films are rather homogeneous. Figure 9a models the activity trends observed in
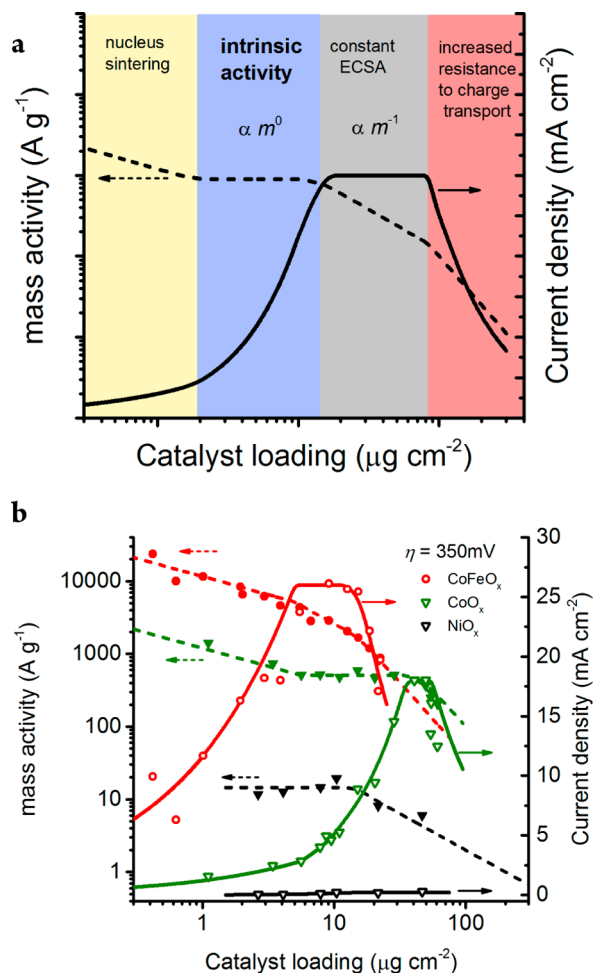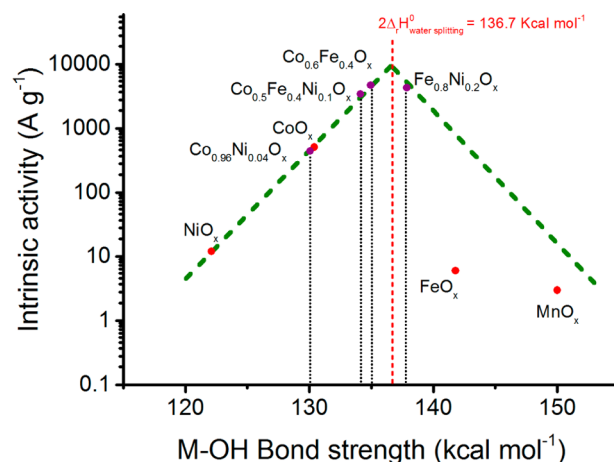

Figure 9. OER activity of transition metal (oxy)hydroxides. (a) Schematic representation of the various regions observed in a log−log plot of activity vs loading. The right axis shows the current density calculated as the product of the mass activity and loading. (b) Fitting of experimental data obtained for the mass activity of metal (oxy)hydroxides.

the log−log plots for the various transition metal oxides. First, at low catalyst loadings, the mass-averaged activity, which is proportional to the apparent TOF, decreases with increasing loading. However, Figure 5b shows that for each catalyst the OER activity is proportional to the electrochemical surface area at all loadings. Thus, the initial decrease in TOF can be attributed to a decrease in the mass-averaged surface area in the first few layers of oxides. Presumably, below monolayer coverage the film first grows on the substrate plane because of the higher conductivity of the substrate compared with the

film itself. The mass-averaged surface area is at its maximum. Beyond monolayer coverage, the film starts to grow on top of the previous layer(s), and the mass-averaged surface area decreases. This process might be considered as "nucleus sintering". Second, at higher loadings the "nucleus sintering" stops and the activity per unit mass is independent of the loading. The values obtained in this region may be considered as a true indicator of the intrinsic activity of the materials, as practical catalysts will have multiple layers. In a third region, the surface area is constant when the mass is increased, and a slope of −1 appears in the log–log plot. A maximum current density is obtained in this region. At even higher loadings, a decrease in activity is observed because of the increased resistance to charge transport in thicker films, which is also reflected in a transmission line in the EIS spectra (e.g., Figure 6d). The decrease in activity at higher loadings is not due to limited hydroxide ion diffusion inside of the pores of the material, as in a diffusion-limited regime the observed current density would be constant. It should be noted that at high catalyst loadings, adhesion of gas bubbles at the surface might affect the observed activity, and the degree of adhesion depends on the morphology and surface aerophobicity.[45,46] In the range of current densities investigated in this study, the activity is not affected by bubble adhesion.

The experimental data in Figure S9 were fitted using the simulated trend in Figure 9a. A good fit over a wide range of loading was obtained (Figure 9b). Table S2 summarizes the intrinsic mass activities of the various transition metal (oxy)hydroxides at η = 350 mV in 1 M KOH. The various transition metal (oxy)hydroxides studied here exhibit different intrinsic activities. Among the unary metal oxides, CoO_x is more active than the Ni, Fe, and Mn oxides by almost 2 orders of magnitude.

The derivation of activity trends for metal oxides has been obscured by the presence of electrolyte impurities, the differences in loading and surface area, and the difficulties in correcting activities for electrical resistance in thick films.[26,27] The log–log plot reported here facilitates the distinction of intrinsic activities from those measured under the influence of morphological and electronic effects. Bockris and Otagawa[47] proposed that although the M−OH bond strength is not a definitive parameter of activity, it should allow the extraction of activity trends for metal oxides.[7,26,27] The bond strength $D(M−OH)$ was defined as the sum of the bond dissociation energies for the heterolytic dissociation $D_{ion}(M−OH)$ and homolytic dissociation $D_{cov}(M−OH)$ of a metal hydroxide of the form $M^{III}(OH)_3$. We attempted to correlate the intrinsic activities of the various transition metal (oxy)hydroxides reported here to M−OH bond strengths of the (oxy)hydroxides as proposed by Bockris and Otagawa (Figure 10). The determination of M−OH bond strengths in binary and ternary oxides is not obvious, so we used the bond strengths of physical mixtures of the corresponding unary hydroxides (Table S3) as approximations. The correlation of the activities of various metal oxides with their M−OH bond strengths gave rise to a volcano-shaped plot. The maximum intrinsic activity is obtained for bond strengths of around 136 kcal mol^{-1} (569.0 kJ mol^{-1}). NiO_x and CoO_x are in the ascending branch where the bond strength is below the optimal value. Because nickel and cobalt are on the same side of the volcano plot, $NiCoO_x$ shows activity proportional to the cobalt content. This implies that there is no significant synergistic effect between nickel and cobalt for the OER. The introduction of iron using the anodic electrodeposition method

Figure 10. Volcano plot of the intrinsic activities of transition metal (oxy)hydroxides vs M−OH bond strength. The green dotted lines indicate a hypothetical, perfect volcano.

reported here results in some of the most active catalysts reported to date. $CoFeO_x$ and $NiCoFeO_x$ show activities similar to those of the previously reported $FeNiO_x$. They are close to the top of the volcano. Because iron oxide is in the opposite branch of the volcano plot relative to NiO_x and CoO_x, its presence alters the electronic properties of the Ni−OH and Co−OH bonds and vice versa. A possible molecular-level explanation was given by Stahl and co-workers,[48] who reasoned that Ni^{3+} has more electrons in π-symmetric (t_{2g}) d orbitals in Fe−O−Ni bonds relative to Fe^{3+} in Fe−O−Fe bonds. This increases the electron-donating ability of the π-symmetric lone pairs of the bridging oxygen, which weakens the Fe−OH bond. This is expected to reduce the potential for the oxidation of Fe^{3+} to Fe^{4+} and increase the $Ni^{2+/3+}$ and $Co^{2+/3+}$ redox potentials. A lower oxidation potential for $Fe^{3+/4+}$ would result in a lower overpotential for the OER at the Fe center.

The optimal M−OH bond strength in Figure 10 is around 136 kcal mol^{-1}, which is close to the total energy required to produce 1 mol of O_2 from 2 mol of water at 298 K (136.7 kcal or 572 kJ). This result could be understood by a thermal cycle analysis of the OER according to the catalytic cycle in Figure S16. According to the analysis, $D(M−OH) = D_{cov}(M−OH) + D_{ion}(M−OH) = \Delta H^{\circ}_{water\ splitting}$ (Figure S16) in a thermoneutral cycle. The optimal bond strength of 136.7 kcal mol^{-1} thus indicates that the best catalyst enables OER in a thermoneutral process. This conclusion is independent of the catalytic mechanism. The thermal cycle analysis also explains why the M−OH bond strength is a good descriptor of the OER activity. Koper and co-workers had used density functional theory calculations to explain the apparent success of bulk thermochemistry as a descriptor of the activity of transition metal oxides for the OER.[49] They found that the bulk thermochemistry and surface absorption energetics depend similarly on the number of outer d electrons in transition metal oxides. The results shown here are in agreement with their finding.

■ CONCLUSION

We have developed a novel electrochemical method for the deposition of a family of thin-film transition metal (oxy)-hydroxides. The electrodeposited thin films contain crystalline nanodomains with lattice spacings similar to those of double-layered hydroxides. These thin films are OER catalysts. The

electrodeposition method allowed precise measurements of catalyst loading and activity. By separation of the contributions of electrochemical surface area and resistance to charge transport within the catalyst films during the OER, the intrinsic activity of the various metal oxyhydroxides was obtained in the form of turnover frequencies and mass-averaged activities. The metal oxyhydroxides can be classified into three categories: $CoFeO_x$, $FeNiO_x$, and $CoFeNiO_x$ belong to the first group, which is most active; CoO_x and $CoNiO_x$ belong to the second group; and NiO_x, FeO_x, and MnO_x belong to the last group, which has only modest activity at modest overpotentials. A volcano correlation of the intrinsic activity with M–OH bond strength could be observed, suggesting the latter as a valid descriptor of the OER activity. The $CoFeO_x$ and $CoFeNiO_x$ catalysts were deposited on high-surface-area electrode Ni foam. In 1 M KOH, the most active $CoFeNiO_x$ catalyst reached current densities of 10 and 100 mA cm^{-2} at overpotentials as low as 240 and 270 mV, respectively. This activity is among the highest for a metal oxide film. The characterization tools presented in this work should facilitate the study and understanding of porous thin-film electrocatalysts.

■ ASSOCIATED CONTENT

Ⓢ Supporting Information

The Supporting Information is available free of charge on the ACS Publications website at DOI: 10.1021/jacs.6b05196.

Additional figures and tables (PDF)

■ AUTHOR INFORMATION

Corresponding Author

*xile.hu@epfl.ch

Notes

The authors declare no competing financial interest.

■ ACKNOWLEDGMENTS

■ REFERENCES

(1) Lewis, N. S.; Nocera, D. G. *Proc. Natl. Acad. Sci. U. S. A.* **2006**, *103*, 15729.

(2) Carmo, M.; Fritz, D. L.; Mergel, J.; Stolten, D. *Int. J. Hydrogen Energy* **2013**, *38*, 4901.

(3) Dau, H.; Limberg, C.; Reier, T.; Risch, M.; Roggan, S.; Strasser, P. *ChemCatChem* **2010**, *2*, 724.

(4) Nakagawa, T.; Beasley, C. A.; Murray, R. W. *J. Phys. Chem. C* **2009**, *113*, 12958.

(5) Sugimoto, W.; Iwata, H.; Yokoshima, K.; Murakami, Y.; Takasu, Y. *J. Phys. Chem. B* **2005**, *109*, 7330.

(6) Gong, M.; Dai, H. *Nano Res.* **2015**, *8*, 23.

(7) Fabbri, E.; Habereder, A.; Waltar, K.; Kotz, R.; Schmidt, T. J. *Catal. Sci. Technol.* **2014**, *4*, 3800.

(8) Yeo, B. S.; Bell, A. T. *J. Am. Chem. Soc.* **2011**, *133*, 5587.

(9) Smith, R. D. L.; Prévot, M. S.; Fagan, R. D.; Zhang, Z.; Sedach, P. A.; Siu, M. K. J.; Trudel, S.; Berlinguette, C. P. *Science* **2013**, *340*, 60.

(10) Kuo, C.-H.; Mosa, I. M.; Poyraz, A. S.; Biswas, S.; El-Sawy, A. M.; Song, W.; Luo, Z.; Chen, S.-Y.; Rusling, J. F.; He, J.; Suib, S. L. *ACS Catal.* **2015**, *5*, 1693.

(11) Doyle, R. L.; Lyons, M. E. G. *J. Electrochem. Soc.* **2013**, *160*, H142.

(12) McCrory, C. C. L.; Jung, S.; Peters, J. C.; Jaramillo, T. F. *J. Am. Chem. Soc.* **2013**, *135*, 16977.

(13) Man, I. C.; Su, H.-Y.; Calle-Vallejo, F.; Hansen, H. A.; Martínez, J. I.; Inoglu, N. G.; Kitchin, J.; Jaramillo, T. F.; Nørskov, J. K.; Rossmeisl, J. *ChemCatChem* **2011**, *3*, 1159.

(14) Trotochaud, L.; Ranney, J. K.; Williams, K. N.; Boettcher, S. W. *J. Am. Chem. Soc.* **2012**, *134*, 17253.

(15) Yeo, B. S.; Bell, A. T. *J. Phys. Chem. C* **2012**, *116*, 8394.

(16) Lower loadings result in higher TOF values because the current density is normalized with respect to the total catalyst loading.

(17) Morales-Guio, C. G.; Mayer, M. T.; Yella, A.; Tilley, S. D.; Grätzel, M.; Hu, X. *J. Am. Chem. Soc.* **2015**, *137*, 9927.

(18) The TOFs for $NiFeO_x$ and $FeNiO_x$ were calculated according to the Ni content. However, recent works have shown that Fe might be the active species. The TOFs should be on the same order of magnitude if the Fe content is used in the TOF calculation.

(19) Batchellor, A. S.; Boettcher, S. W. *ACS Catal.* **2015**, *5*, 6680.

(20) Trotochaud, L.; Young, S. L.; Ranney, J. K.; Boettcher, S. W. *J. Am. Chem. Soc.* **2014**, *136*, 6744.

(21) Gileadi, E. *Physical Electrochemistry: Fundamentals, Techniques and Applications*; Wiley-VCH: Weinheim, Germany, 2011.

(22) Biesinger, M. C.; Payne, B. P.; Grosvenor, A. P.; Lau, L. W. M.; Gerson, A. R.; Smart, R. S. C. *Appl. Surf. Sci.* **2011**, *257*, 2717.

(23) Boroďko, Y. G.; Vetchinkin, S. I.; Zimont, S. L.; Ivleva, I. N.; Shul'ga, Y. M. *Chem. Phys. Lett.* **1976**, *42*, 264.

(24) Esswein, A. J.; McMurdo, M. J.; Ross, P. N.; Bell, A. T.; Tilley, T. D. *J. Phys. Chem. C* **2009**, *113*, 15068.

(25) Klingan, K.; Ringleb, F.; Zaharieva, I.; Heidkamp, J.; Chernev, P.; Gonzalez-Flores, D.; Risch, M.; Fischer, A.; Dau, H. *ChemSusChem* **2014**, *7*, 1301.

(26) Burke, M. S.; Zou, S.; Enman, L. J.; Kellon, J. E.; Gabor, C. A.; Pledger, E.; Boettcher, S. W. *J. Phys. Chem. Lett.* **2015**, *6*, 3737.

(27) Burke, M. S.; Enman, L. J.; Batchellor, A. S.; Zou, S.; Boettcher, S. W. *Chem. Mater.* **2015**, *27*, 7549–7558.

(28) Friebel, D.; Louie, M. W.; Bajdich, M.; Sanwald, K. E.; Cai, Y.; Wise, A. M.; Cheng, M.-J.; Sokaras, D.; Weng, T.-C.; Alonso-Mori, R.; Davis, R. C.; Bargar, J. R.; Nørskov, J. K.; Nilsson, A.; Bell, A. T. *J. Am. Chem. Soc.* **2015**, *137*, 1305.

(29) Burke, M. S.; Kast, M. G.; Trotochaud, L.; Smith, A. M.; Boettcher, S. W. *J. Am. Chem. Soc.* **2015**, *137*, 3638.

(30) Klaus, S.; Cai, Y.; Louie, M. W.; Trotochaud, L.; Bell, A. T. *J. Phys. Chem. C* **2015**, *119*, 7243.

(31) Doyle, R. L.; Lyons, M. E. G. *Phys. Chem. Chem. Phys.* **2013**, *15*, 5224.

(32) Gabrielli, C.; Haas, O.; Takenouti, H. *J. Appl. Electrochem.* **1987**, *17*, 82.

(33) Vrubel, H.; Moehl, T.; Gratzel, M.; Hu, X. *Chem. Commun.* **2013**, *49*, 8985.

(34) Bisquert, J. *J. Phys. Chem. B* **2002**, *106*, 325.

(35) Bisquert, J.; Grätzel, M.; Wang, Q.; Fabregat-Santiago, F. *J. Phys. Chem. B* **2006**, *110*, 11284.

(36) Bediako, D. K.; Costentin, C.; Jones, E. C.; Nocera, D. G.; Savéant, J.-M. *J. Am. Chem. Soc.* **2013**, *135*, 10492.

(37) The resistor R_m in the EIS model is related to the ease with which charges can move through the film through a diffusion-like process. The concentration of positive charges is highest at the back contact and decreases along the length of the film as a result of their leakage to the active sites and the electrolyte to evolve oxygen.

(38) Gong, M.; Li, Y.; Wang, H.; Liang, Y.; Wu, J. Z.; Zhou, J.; Wang, J.; Regier, T.; Wei, F.; Dai, H. *J. Am. Chem. Soc.* **2013**, *135*, 8452.

(39) Tench, D.; Warren, L. F. *J. Electrochem. Soc.* **1983**, *130*, 869.

(40) Therese, G. H. A.; Kamath, P. V. *Chem. Mater.* **2000**, *12*, 1195.

(41) Corrigan, D. A. *J. Electrochem. Soc.* **1987**, *134*, 377.

(42) Lu, X.; Zhao, C. *Nat. Commun.* **2015**, *6*, 6616.

(43) Brownson, J. R. S.; Lévy-Clément, C. *Phys. Status Solidi B* **2008**, *245*, 1785.

(44) Uudsemaa, M.; Tamm, T. *J. Phys. Chem. A* **2003**, *107*, 9997.

(45) Lu, Z.; Xu, W.; Zhu, W.; Yang, Q.; Lei, X.; Liu, J.; Li, Y.; Sun, X.; Duan, X. *Chem. Commun.* **2014**, *50*, 6479.

(46) Lu, Z.; Zhu, W.; Yu, X.; Zhang, H.; Li, Y.; Sun, X.; Wang, X.; Wang, H.; Wang, J.; Luo, J.; Lei, X.; Jiang, L. *Adv. Mater.* **2014**, *26*, 2683.

(47) Bockris, J. O. M.; Otagawa, T. *J. Electrochem. Soc.* **1984**, *131*, 290.

(48) Chen, J. Y. C.; Dang, L.; Liang, H.; Bi, W.; Gerken, J. B.; Jin, S.; Alp, E. E.; Stahl, S. S. *J. Am. Chem. Soc.* **2015**, *137*, 15090.

(49) Calle-Vallejo, F.; Díaz-Morales, O. A.; Kolb, M. J.; Koper, M. T. M. *ACS Catal.* **2015**, *5*, 869.